Journal of Hazardous Materials 441 (2023) 129940

Contents lists available at ScienceDirect

Journal of Hazardous Materials

journal homepage: www.elsevier.com/locate/jhazmat

# Selective production of singlet oxygen for harmful cyanobacteria inactivation and cyanotoxins degradation: Efficiency and mechanisms

Bingzhi Yu [a], Xizi Li [a], Mengfan He [a], Yan Li [a], Jiafeng Ding [a,b,*], Yuchi Zhong [a,b], Hangjun Zhang [a,b,*]

[a] School of Life and Environmental Sciences, Hangzhou Normal University, 311121 Hangzhou, Zhejiang, China
[b] School of Engineering, Hangzhou Normal University, 311121 Hangzhou, Zhejiang, China

## HIGHLIGHTS

- The feasibility of inactivating four harmful cyanobacteria was investigated.
- $^1O_2$ played a major role in efficiently removing *M. aeruginosa* and *MC-LR*.
- Changes in the extracellular morphology of cyanobacteria were observed via SEM.
- Eight degradation intermediates of MC-LR were identified.
- A potential mechanism for cyanobacteria inactivation was proposed.

## GRAPHICAL ABSTRACT

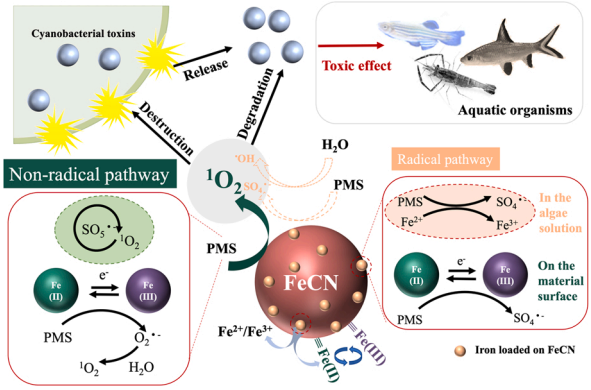


## ARTICLE INFO

Editor: Danmeng Shuai

*Keywords:*
Singlet oxygen
Peroxymonosulfate
Microcystis aeruginosa
Cyanobacterial toxins
Degradation pathway

## ABSTRACT

Knowledge about the impact of singlet oxygen ($^1O_2$) on the characteristics and inactivation of harmful cyanobacterial organic matter is limited. In this study, the feasibility of using an improved single-iron doped graphite-like phase carbon nitride catalyst (FeCN) to activate peroxymonosulfate (PMS) catalytic production of $^1O_2$ to inactivate four harmful cyanobacteria was investigated. The inactivation efficiencies at 30 min were 92.77%, 66.84%, 91.06%, and 93.45% for *Microcystis aeruginosa* (*M. aeruginosa*), *Nodularia harveyana*, *Oscillatoria* sp., and *Nostoc* sp., respectively. This was associated with adjusting experimental parameters, such as the FeCN and PMS doses and initial pH, to obtain the maximum $^1O_2$ yield. The quenching experiment results and electron paramagnetic resonance spectra showed that $^1O_2$ generated via the non-radical pathway might play a dominant role in inactivating harmful cyanobacteria and degrading harmful algal toxins (Microcystin-LR and Nodularin). In addition, the FeCN-PMS system not only effectively destroyed the integrity of harmful cyanobacterial cells but also effectively degraded cyanobacterial toxins, thereby preventing severe secondary contamination by cell rupture. A possible removal mechanism was proposed. This reveals the potential of $^1O_2$ to simultaneously inactivate harmful cyanobacteria and degrade harmful cyanobacterial toxins.

* Corresponding authors at: School of Life and Environmental Sciences, Hangzhou Normal University, 311121 Hangzhou, Zhejiang, China
*E-mail addresses:* djf101@126.com (J. Ding), 13819172516@163.com (H. Zhang).

https://doi.org/10.1016/j.jhazmat.2022.129940
Received 28 July 2022; Received in revised form 26 August 2022; Accepted 5 September 2022
Available online 8 September 2022

## 1. Introduction

The occurrence of harmful algal blooms (HABs) in source water is a growing global problem. During algal blooms, harmful cyanobacteria occupy the habitat of other organisms. Consequently, biological community structure and ecological balance in aquatic environments become disrupted and biodiversity decreases (Guo et al., 2021; Ho et al., 2019; Huisman et al., 2018). Algal toxins released by harmful cyanobacteria also affect other organisms and cause damage to human kidneys, lungs, and other organs via the amplification effect in food chains (He et al., 2021; Zhu et al., 2021). Hence, the management of harmful cyanobacterial blooms has received considerable research attention. However, conventional algae removal processes break algal cells, which leads to the unavoidable release of algal toxins (Huo et al., 2015; Jeon et al., 2015; Paerl et al., 2016). Considering this, the best way to overcome the problem of high levels of algal toxins is via the simultaneous removal of algal toxins and algal cell fragmentation. Fan et al. (2020) prepared a novel photocatalytic coating $Ag_2CO_3$-N:GO for photocatalytic inactivation of *M. aeruginosa* and degradation of MC-LR. Chitosan/Graphene (CSG) Composites used to Evaluate Removal of Cyanobacteria and Cyanotoxins (Zetterholm et al., 2022).

To date, the application of heterogeneous activation of peroxymonosulfate (PMS) to generate singlet oxygen ($^1O_2$) remains a promising method because of its high efficiency, environmental friendliness, and low cost. Owing to its unoccupied π * orbitals, $^1O_2$ exhibits greater resistance to environmental interference and degradation selectivity for materials such as antibiotics (Fang et al., 2022; He et al., 2022), unsaturated molecules (Di Mascio et al., 2019), and microbial pathogens (Hamblin, 2016) than that of $^{\bullet}OH$ and $SO_4^{\bullet -}$. The main pathways of singlet oxygen generation include (i) photosensitizers reaching the excited state by absorbing ultraviolet (UV) or visible light and transferring energy to the surrounding $O_2$ producing $^1O_2$ (Yaraki et al., 2022) and (ii) $^1O_2$ being produced through the intermediates $O_2^{\bullet -}$ and $SO_5^{\bullet -}$, which are precursors for $^1O_2$ production. Moreover, the presence of Fe–N bonds reportedly drive the formation of $^1O_2$ from $SO_5^{\bullet -}$ (Li et al., 2020b; Zhang et al., 2021). (iii) Special structures in catalytic materials, such as those produced as a result of the introduction of oxygen vacancies, doping of metal particles, and construction of domain-limited spaces, promote $^1O_2$ production. For example, Liu et al. (2018) used $Bi_{25}FeO_{40}$ to activate PMS for degrading levofloxacin and found that oxygen vacancies could directly produce $^1O_2$. The doping of metal particles into catalytic materials by various ways can improve the electronic state and coordination environment at their surfaces, resulting in the effective production of $^1O_2$ (Mi et al., 2021).

$^1O_2$ has recently been shown to be effective in treating novel pollutants under dark–light anoxic conditions, owing to its strong oxidizing properties, its relatively longer half-life, it being relatively less influenced by the substrate/water interface and water quality levels, and relatively low susceptibility to quenching (Miao et al., 2019). In particular, the activation of persulfate (PS) to produce $^1O_2$ by homogeneous and heterogeneous phases facilitates the efficient removal of pollutants. Yan et al. (2016) found that the Fe(II) and Fe(II) to Fe(III) transition at the surface of $Fe_3O_4$ nanoparticles catalyze the production of both $SO_4^{\bullet -}$ and $^1O_2$ by PS. Zhao et al. (2021a) concluded that the doping of Sr effectively accelerates electron transfer between Fe and PMS in $LaFeO_3$, thereby generating a large amount of $O_2^{\bullet -}$ and $^1O_2$ to achieve organic matter degradation. Xiao et al. (2018) revealed that surface electron donor groups, defective edges, oxygen-containing functional groups (-COOH, C–OH, -OH, and C═O), $sp^2$ hybridized carbon, and delocalized π-electrons are important factors influencing the catalytic PS generation of $^1O_2$ from carbon materials. Specifically, Single-atom catalysts have been used to activate PMS to generate $^1O_2$ due to their higher selectivity and efficiency (Zhao et al., 2021b). N-doped carbon supported single-atom catalysts have exhibited significantly enhanced $^1O_2$ generation selectivity from the activated PMS. In addition, graphite-like phase carbon nitride (g-CN) possesses specific C and N sites and high N content, resulting in abundant and homogeneous single-atom immobilization sites (Chen et al., 2020; Sun et al., 2022). Zhang et al. (2021) concluded that the $Fe_1$/CN catalysts having a highly uniform Fe-$N_4$ structure, which was used to activate PMS to generated $^1O_2$ at 100% selectivity to achieve organic matter degradation. Therefore, the application of Fe single-atom doped g-CN (FeCN) of heterogeneous PMS activation to generate $^1O_2$ for studying the inactivation of harmful cyanobacteria shows good development prospects and potential.

In this study, an improved FeCN with high dispersibility was successfully prepared and evaluated for the heterogeneous activation of PMS to inactivate *Microcystis aeruginosa*, *Nodularia harveyana*, *Oscillatoria* sp., and *Nostoc* sp. and degrade algal toxins, including dose, humic acid, and pH effects. Finally, the possible mechanisms of cyanobacterial inactivation and algal toxin degradation by FeCN-activated PMS were investigated. This study proposes an efficient and environment-friendly method for simultaneously inactivating harmful cyanobacteria and degrading algal toxins, thereby providing a reference basis for the treatment of harmful cyanobacterial blooms.

## 2. Materials and methods

### 2.1. Chemicals used and algal preparation

Melamine ($C_3H_6N_6$) and cyanuric acid ($C_3H_3N_3O_3$) were obtained from Aladdin Reagent (China). Ethanedioic acid dihydrate ($C_2H_2O_4$0.2 $H_2O$) and $Fe(NO_3)_3$0.9 $H_2O$ were obtained from the SCR (China). Potassium monopersulfate triple salt ($K_5H_3S_4O_{18}$ [42–46% $KHSO_5$ basis]) and L-histidine ($C_6H_9N_3O_2$) were obtained from Macklin (China). Acetonitrile ($CH_3CN$, gradient grade for liquid chromatography) and methanol ($CH_4O$, ≤100%, gradient grade for liquid chromatography) were purchased from Merck (Germany). $H_2SO_4$, NaOH, $HNO_3$, pentanediol ($C_5H_{12}O_2$), ethanol ($C_2H_6O$, EtOH), isopropanol (IPA), furfuryl alcohol, and tert-butanol were obtained from Sinopharm Chemical Reagent Co. Ltd. (China). NOD was obtained from Enzo Biochem (USA). Ultrapure water with a resistance of 18.2 MΩ-cm was prepared using a water purification device (Direct-Q 3UV, USA).

*M. aeruginosa* (No. FACHB-905), *N. harveyana* (No. FACHB-1490), *Oscillatoria* sp. (No. FACHB-528), and *Nostoc* sp. (No. FACHB-131) were provided by the Institute of Aquatic Biology, Chinese Academy of Sciences (Hubei, China). The cells were cultured in a BG11 medium under the following conditions: light intensity of 3000 lx and light–dark ratio of 12 h:12 h. The algal cultures were shaken daily.

### 2.2. Preparation of g-CN and FeCN

FeCN and g-CN were prepared via a conventional thermal polymerization method (Guo et al., 2016; Zhang et al., 2021). First, $C_3H_6N_6$ (30 mM) and $C_3H_3N_3O_3$ (24 mM) were dissolved in 100 mL of ultrapure water at 85 °C and stirred for 30 min. Appropriate amounts of Fe $(NO_3)_3$0.9 $H_2O$ and $C_2H_2O_4$0.2 $H_2O$ were dissolved in 50 mL of ultrapure water at 25 ± 1 °C. The above two solutions were mixed and stirred at room temperature for 4 h, collected by centrifugation, and dried overnight at 60 °C. Thereafter, calcination was conducted under nitrogen atmosphere at 520 °C for 2 h at a heating rate of 5 °C·$min^{-1}$ to obtain FeCN. g-CN was prepared similarly but without adding $Fe(NO_3)_3$0.9 $H_2O$ and $C_2H_2O_4$0.2 $H_2O$.

### 2.3. Characterization

X-ray diffraction (XRD) maps were obtained on a Bruker D8 ADVANCE A25X at 40 kV and 40 mA at a scan rate of 5° $min^{-1}$ over a 2θ range of 5–60°. Fourier-transform infrared spectroscopy (FTIR, BRUKER TENSOR 27, Germany) was used to analyze the structural information of the catalyst samples. The BET-specific surface area method was used to categorize nitrogen adsorption on materials. X-ray photoelectron

spectroscopy (XPS) analysis was performed using a spectrometer (Thermo Fisher Scientific, USA) with Al Kα anodic radiation as the source (1486.8 eV). All binding energies were referenced to the C 1 s peak at 284.8 eV. Free radicals were recorded on an electron paramagnetic resonance (EPR) spectrometer (JES-FA 300, Japan) using 50.0 mM of DMPO and TEMP as spin traps. Scanning electron microscopy (SEM) was performed using a Zeiss Sigma 300 microscope at 10 kV. Transmission electron microscopy images were obtained using a Tecnai F20 microscope at 200 kV.

### 2.4. Experimental procedures

An algal solution with an initial chlorophyll-*a* concentration of 0.60 $mg{\cdot}L^{-1}$ was prepared. Before the test, 0.1 M of $H_2SO_4$ and 0.1 M of NaOH were used to adjust the pH of the algal solution to 7.0. The required amounts of FeCN (20 mg) and PMS (0.33 mM) were added to the prepared algal solution (50 mL) and thoroughly shaken. Sampling was done after the resuspension of the algal solution for subsequent experiments and testing. All samples were further analyzed after centrifugation at 4 °C and 4000 rpm for 10 min using a high-speed freezing centrifuge (KDC-140HR). Three parallel trials were performed to obtain the mean ± standard deviation. Except for the individual experiments, the experimental subjects were *M. aeruginosa.*

In addition, optimal doses of FeCN and PMS were used. Orthogonal experimental groups were set up with FeCN concentrations of 0.1, 0.2, 0.3, and 0.4 $g{\cdot}L^{-1}$ and PMS concentrations of 0.16, 0.33, 0.50, and 0.65 mM. A series of experiments were conducted at initial pH values of 5.0, 6.0, 7.0, 8.0, 9.0, and 10.0 to evaluate the effect of pH on inactivation efficiency. In addition, 20.0 mM of TBA, MeOH, IPA, $C_2H_6O$, FFA, and L-histidine were added to quench $SO_4^{\bullet -}$, $^{\bullet}OH$, and $^1O_2$.

### 2.5. Analytical methods

The inactivation efficiency of cyanobacteria was indicated by the changes in chlorophyll-*a* during testing. Samples were repeatedly frozen and thawed in an ice bath. Extractions were then performed using a 95.0% $C_2H_6O$ solution, and absorbance was measured at wavelengths of 665 and 649 nm using a UV spectrophotometer (UV-1800, Shimadzu). The chlorophyll-*a* concentrations can be calculated as follows (Song et al., 2020):

$$C_{chl\text{-}a}=13{\cdot}95A_{665}-6{\cdot}88A_{649}$$

$$R\ (\%)=(C_{Chla0}\text{-}C_{Chlat})/C_{Chla0}\times 100\%$$

where $C_{Chla0}$ and $C_{Chlat}$ are the concentrations of chlorophyll-*a* initially and after treatment, respectively.

The $UV_{254}$ value represents the amount of naturally occurring humic macromolecular organic matter and aromatic compounds containing C═C and C═O in water (Xia et al., 2018). Therefore, it characterizes the extravasation of intracellular organic matter.

Algal organic matter (AOM) was analyzed to explore the inactivation effect of cyanobacteria. The samples were measured using a fluorescence spectrophotometer (F-4600, Thermo Fisher Scientific) to obtain excitation–emission matrix spectra (EEM). Blank correction was performed using the fluorescence spectra of ultrapure water, and the following parameters were set: the PMT voltage was set to 700 V; and excitation and emission slits, scan rate, excitation wavelength range, and emission wavelength range were 5 nm, 12,000 $nm{\cdot}min^{-1}$, 200–450 mm, and 200–550 nm, respectively (Yu et al., 2019; Zhang et al., 2022).

The samples were acidified to pH< 2 using $HNO_3$ passed over a membrane (0.45 μm). Fe(II) was then detected via the o-phenanthroline method, and the total iron content was determined via ICP-MS (NexION 1000 G, PerkinElmer, USA).

The samples were fixed overnight with 2.5% $C_5H_{12}O_2$ and dehydrated using a gradient of $C_2H_6O$ and water mixture and finally 100% $C_2H_6O$. The algal cells were observed via SEM after vacuum freeze-drying.

The cultured *M. aeruginosa* could produce MC-LR; therefore, the original algal solution was used for the algal toxin degradation experiments. In addition, a simulated algal solution with an initial NOD concentration of 50 $\mu g{\cdot}L^{-1}$ was prepared. The samples were analyzed via UPLC-MS/MS (Xevo TQ-S, Waters, USA) (Jimenez et al., 2020), and the mobile phase was a mixture of water and acetonitrile at a ratio of 65:35 (v/v). The C18 column temperature was 40 °C. The detection wavelength was set at 238 nm. MC-LR degradation intermediates in the *m/z* range of 200–1000 were obtained and analyzed via MS scanning (continuum mode) from 0 to 20 min

## 3. Results and discussion

### 3.1. Inactivation of harmful cyanobacteria

The removal efficiency of chlorophyll-*a* was used to evaluate the inactivation effect of an FeCN-PMS system on cyanobacteria. In addition, the absorbance of the sample at 254 nm was measured as a reference for the inactivation effect. Fig. 1a shows the inactivation effect of *M. aeruginosa* using different additives. After adding FeCN or PMS alone, there was little change in the algal solution, and the maximum inactivation efficiencies were only 3.91% and 11.36%, respectively, in 30 min. This indicates that FeCN and PMS are almost harmless to algal cells. The simultaneous addition of FeCN and PMS to the algal solution resulted in significant changes in the algal solution, with the inactivation rate reaching 71.55% at 5 min and 92.77% at 30 min. As shown in Fig. 1b, the inactivation efficiencies of *Nodularia harveyana*, *Oscillatoria* sp., and *Nostoc* sp. were 66.84%, 91.06%, and 93.45%, respectively, at 30 min. The differences in inactivation effects may be due to the different structural and physiological adaptations of the algae (Chu et al., 2022; Perillo et al., 2022); however, further studies are required to clarify this. Overall, the test verified the possibility that FeCN-PMS could simultaneously inactivate multiple cyanobacteria.

Fig. 2 shows the inactivation efficiency of *M. aeruginosa* at different FeCN and PMS ratios. As shown in Fig. 2a, the algal inactivation rate increased from 32.22% to 99.04% with the increase in the dose of FeCN (or PMS) from 0.1 $g{\cdot}L^{-1}$ (0.16 mM) to 0.4 $g{\cdot}L^{-1}$ (0.65 mM). In contrast, at doses of FeCN < 0.2 $g{\cdot}L^{-1}$ (or PMS < 0.32 mM), the algal inactivation efficiency did not significantly increase, despite the continuous increase in the PMS (or FeCN) dose. Briefly, the inactivation efficiency did not depend solely on the increase in individual additives. When the FeCN dose is relatively low, PMS may not be effectively activated. When the PMS dose is relatively low, less reactive oxygen species (ROS) were produced, and the oxidative stress response of algae may counteract these effects, thereby resulting in a low inactivation efficiency (Yan et al., 2022). The response surface is also represented as a curved surface (Fig. 2b) that demonstrates that the system requires the synergistic effect of FeCN and PMS. Furthermore, the tilt angle of the response surface decreased with an increase in the FeCN (or PMS) dose. Briefly, there is an inactivation threshold for FeCN-PMS because some by-products of the algae also consumed ROS. When this inactivation threshold was reached, the FeCN (or PMS) dose was no longer the major factor affecting the deactivation efficiency. Consequently, FeCN and PMS doses were screened at 0.4 $g{\cdot}L^{-1}$ and 0.33 mM, respectively.

As shown in Fig. 3a, $UV_{254}$ value increased with time after the addition of PMS alone, likely because PMS, being a strong oxidant, had harmful effects on *M. aeruginosa*. The change in $UV_{254}$ value under the FeCN-PMS system also showed the same trend as that of the inactivation efficiency, indicating that the algal cell membranes were disrupted and humic substances were released. This phenomenon can be attributed to the high $S_{BET}$ of FeCN (56.09 $m^2{\cdot}g^{-1}$, Table S1), which may have more active sites to stimulate PMS to produce ROS (i.e., $SO_4^{\bullet -}$, $^{\bullet}OH$, $O_2^{\bullet -}$, and $^1O_2$) that have harmful effects on algal cells. This has been confirmed in previous studies, that revealed the inactivation of *M. aeruginosa* by N-doped $TiO_2$ visible-light-driven generation of free radicals (Zhou et al.,

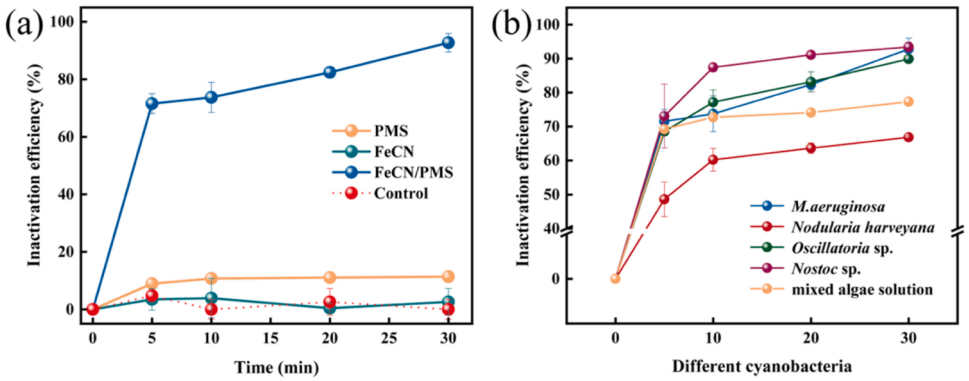


**Fig. 1.** Typical time courses for the a) inactivation efficiency under different additive conditions and (b) inactivation efficiency of different cyanobacteria at 25 ± 1 °C. The reacted solution initially contains approximately 0.60 mg·L$^{-1}$ of chlorophyll-*a*, 0.4 g·L$^{-1}$ of FeCN, and 0.33 mM of PMS.

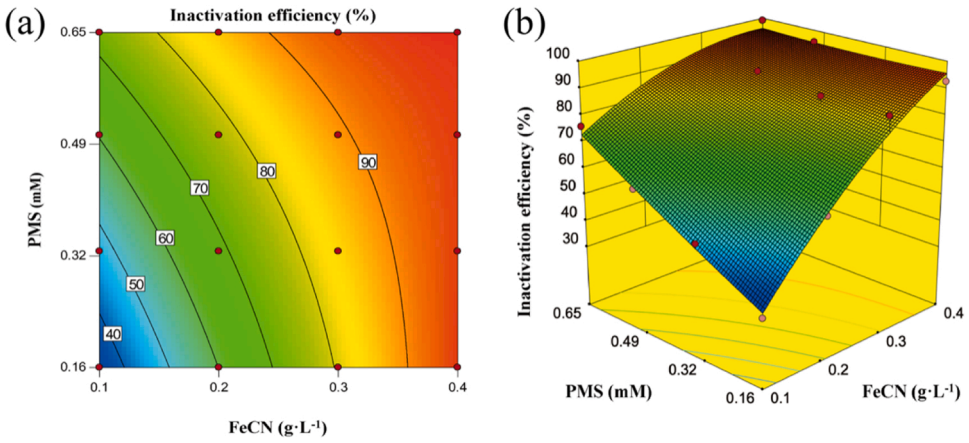


**Fig. 2.** Effects of different dosage ratios on the inactivation efficiency of algae: (a) counter and (b) response surface.

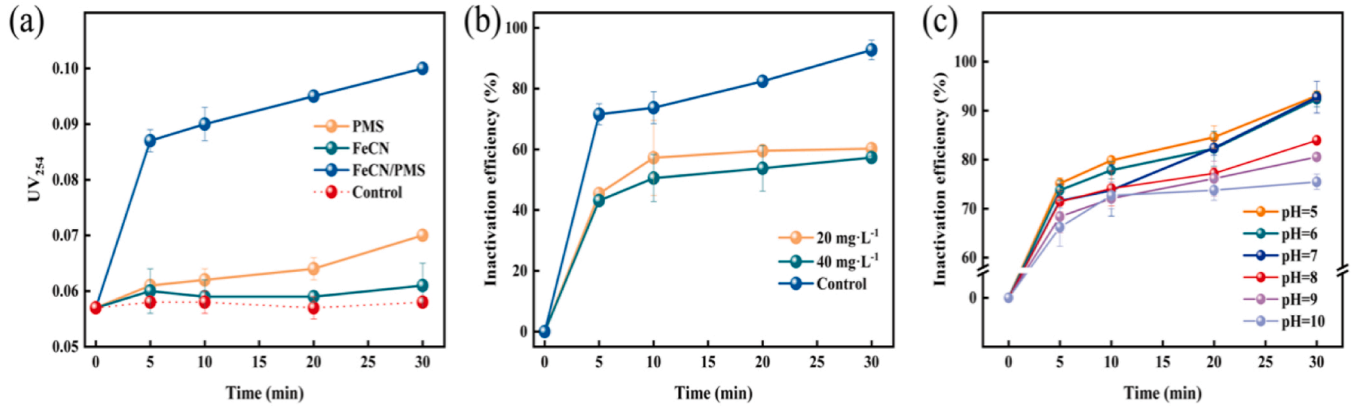


**Fig. 3.** (a) $UV_{254}$ by an FeCN-PMS system. Effects of an FeCN-PMS system on the inactivation efficiency of algae under different (b) humic acid and (c) pH.

2020); hydroxyl radicals and organic radicals play a major role in the combined inactivation of *M. aeruginosa* by peroxyacetic acid and UV light (Cao et al., 2022). In addition, humic acid reportedly react with radicals ($SO_4^{\bullet-}$ and $^{\bullet}OH$), thereby influencing PMS activation (Hoang et al., 2022; Wang et al., 2019; Wang and Wang, 2022). The humic acid released after algal cell rupture may affect the FeCN-PMS system. As shown in Fig. 3b, the inactivation efficiency was reduced by adding high concentrations of humic acid; however, the inactivation effect was > 50%. On the one hand, this is a possible reason for the slow inactivation rate in the middle and later stages of the reaction. On the other hand, the relatively high inactivation effect can be attributed to the greater resistance of $^1O_2$ to humic acid interference. The feasibility of using FeCN-PMS in different algae-containing water matrices was evaluated. The results of the pH effects showed that FeCN-PMS maintained high inactivation rates (> 92.3%) in both medium-acidic environments and remained high (> 75.4%) under alkaline conditions, although the inactivation rates were reduced (Fig. 3c). This phenomenon can be primarily attributed to the following factors: on the one hand, for catalysts, acidic conditions prevent Fe(II) and Fe(III) hydroxides from covering the material surface and promote the continued release of Fe(II) from the material, which enhances PMS activation (Zheng et al., 2022). On the other hand, even under alkaline conditions,

a part of the $SO_4^{\bullet -}$ starts to react with hydroxide ions in water forming $^{\bullet}OH$, and $^1O_2$ may continue to play a major role in the inactivation of cyanobacterial cells (Liu et al., 2022).

### 3.2. Cell morphology and organic matter

The changes in algal cell morphology and integrity imply the rupture of algal cells, which may release large amounts of AOM. Therefore, to investigate the effect of the FeCN-PMS system on extracellular organic matter (EOM), EEM was used to assess the changes in the EOMs using the FeCN-PMS system. As shown in Fig. S1, regions I and II represent aromatic proteins (peak $T_2$, Ex/Em=250/336 nm), region III represents fulvic acid-like proteins (peak A, 275/425 nm), region IV represents soluble microbial by-product-like proteins (peak $T_1$, 280/300 nm), and region V represents humic acid-like proteins (peak C, 350/430 nm) (Chen et al., 2003; Huang et al., 2021b; Li et al., 2020a). In contrast the control (Fig. S1a), the peaks $T_2$, C, and A were significantly high in the FeCN-PMS system (Fig. S1b–d), indicating that the algal microbial cells gradually ruptured releasing intracellular materials; the decrease in the peak $T_1$ may be due to the preferential degradation of soluble microbial by-products by ROS generated in the FeCN-PMS system. However, compared with the results for FeCN alone (Fig. S1e), the decrease in peak $T_1$ could also be attributed to FeCN adsorption. The BET results also showed that FeCN exhibited good adsorption (Fig. 5c). In particular, the peak $T_2$ in the FeCN-PMS system (Fig. S1b–d) was lower than that in the PMS system alone (Fig. S1f). This may be due to the physiological release of a large number of protein compounds under PMS owing to the protection mechanism of the algal cells themselves; however, the algal cells did not die completely. Moreover, they were likely oxidized by the ROS generated by the FeCN-PMS system because of their strong hydrophilicity and poor aggregation ability (Fan et al., 2022).

The changes in the extracellular morphology of the cyanobacteria were observed via SEM. As shown in Fig. 4a–c, the *M. aeruginosa* cells were intact and smooth and contained some secretory material in the control. After FeCN-PMS treatment, irregular cellular deformation and even cell rupture were observed (red circles). As shown in Fig. 4d–f, for multicellular cyanobacteria (e.g., *Nostoc* sp.), after treatment with the FeCN-PMS system, the multicellular chain structure was disrupted, and the cell membrane was destroyed (red circle).

### 3.3. Role of iron species and ROS in the FeCN-PMS system

#### 3.3.1. Role of iron species

Iron species possess redox reactive, including aqueous iron and iron-loaded at the surface of the material (Huang et al., 2021a). The crystal structures of pure g-CN and FeCN were analyzed via XRD, with diffraction peaks located at 13.0° and 27.6° (Fig. 5a), indicating the successful doping of Fe into the g-CN. The $S_{BET}$ of FeCN was 56.09 $m^2 \cdot g^{-1}$ (Table S1), which is much larger than those prepared by other methods:14.7 $m^2 \cdot g^{-1}$ (Mao et al., 2022), 13.65 $m^2 \cdot g^{-1}$ (Zhao et al., 2022), and 34.75 $m^2 \cdot g^{-1}$ (Zhang et al., 2022). Therefore, FeCN possesses high dispersibility and can provide more active sites to activate PMS. XPS analysis results are shown in Fig. S4. The proportion of Fe element was 15.2%. In Fig. S4d, 710.5 and 713.1 eV correspond to the two states of trivalent iron in the Fe–N bond and trivalent iron in ferric oxide, respectively (Liu et al., 2016; Peng et al., 2022), and the peak at

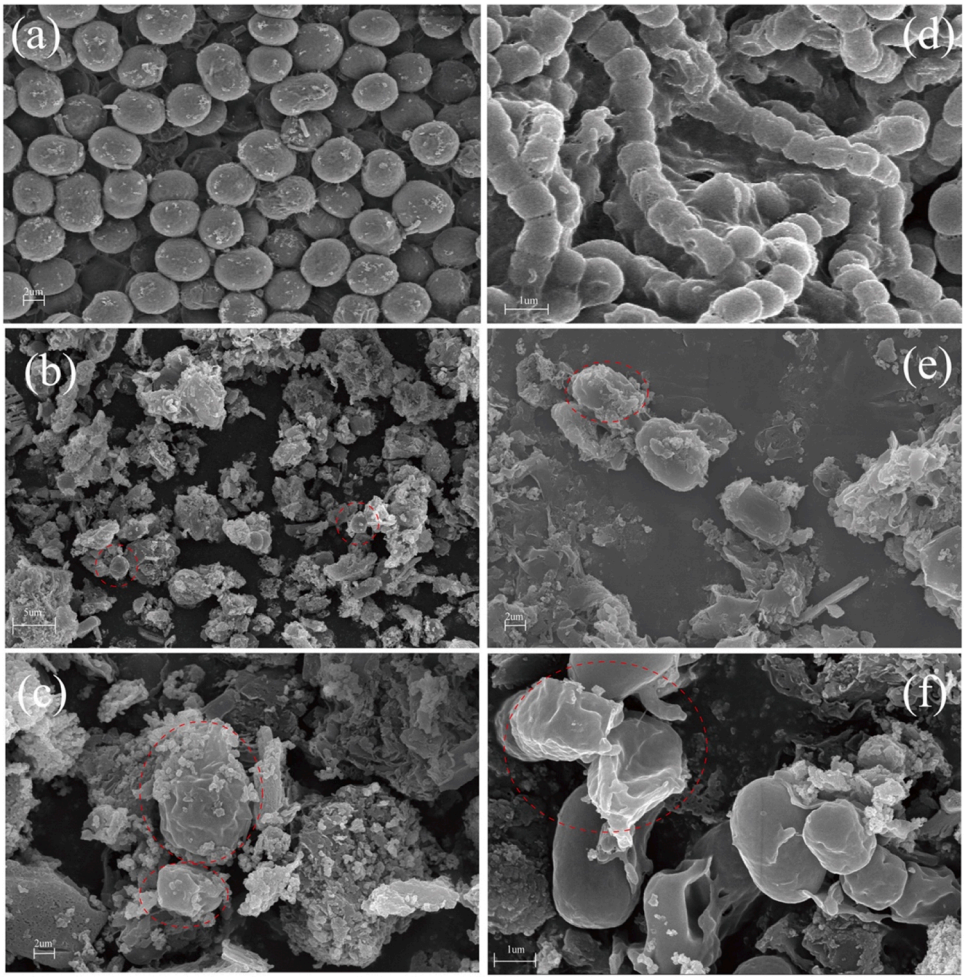


**Fig. 4.** SEM images of the surface morphology of (a–c) *M. aeruginosa* and (d–f) *Nostoc* sp. before and after treatment under the FeCN-PMS system.

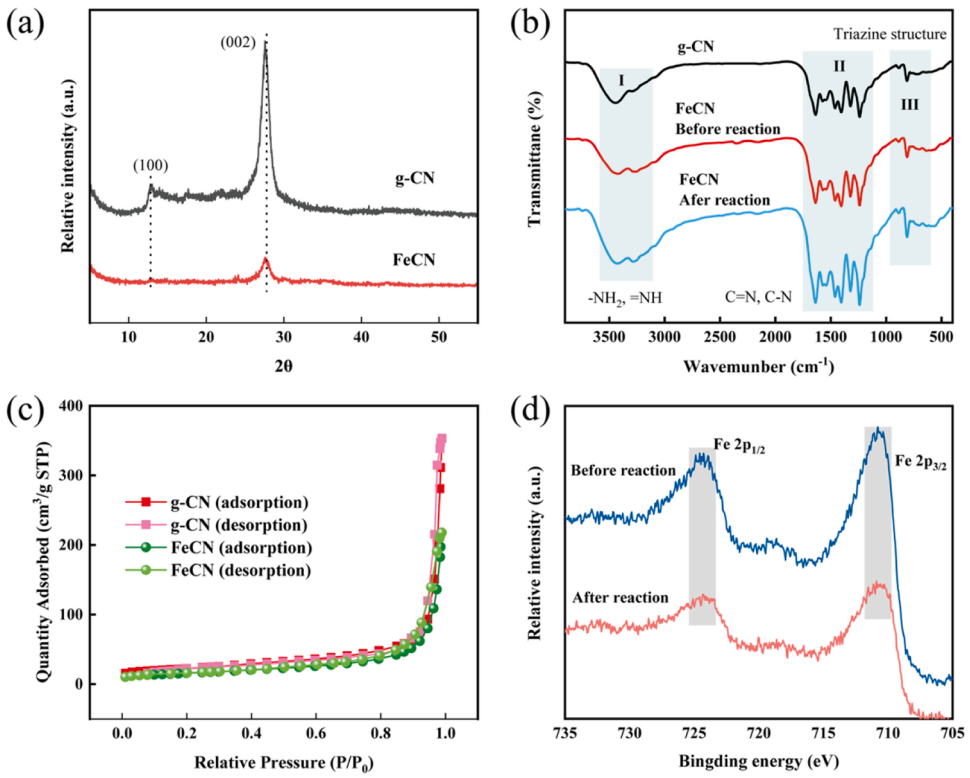


**Fig. 5.** (a) XRD patterns, the ATR-FTIR spectra, and (c) Adsorption/desorption isotherm of the as-prepared samples; (d) Fe 2p XPS spectra of FeCN before and after reaction.

718.6 eV is the satellite peak of trivalent iron. Tan (2016) found that the binding energy of trivalent tetrahedral iron in γ-$Fe_2O_3$ is 713.7 eV; therefore, it can be inferred that Fe–N coordination bonds and ferric oxide are present in FeCN. The XPS results (Fig. 5d) also show a decrease in the peak areas of Fe loaded in FeCN after the reaction which is consistent with the results shown in Fig. S2. Other characterization analyses are in Supporting Information Text S1. The g-CN and FeCN samples were observed v electron microscopy. As shown in Fig. S3a–b, g-CN surface was smooth and free of impurities, whereas FeCN surface was rough with irregular particle aggregation. The granular iron species loaded onto the g-CN are shown in Fig. S3c. Fe elements, other than C and N, were also identified via elemental mapping (Fig. S3d). Considering Fe solubility (Duan et al., 2021), the concentration of dissolved Fe ions in the FeCN-PMS system is shown in Fig. S2. The total Fe ion concentration in the aqueous solution increased to the maximum concentration of 0.23 mg $L^{-1}$ at 30 min. However, $Fe^{2+}$ concentration was maintained at 0.11 mg $L^{-1}$, indicating that $Fe^{2+}$ may reach dissolution equilibrium under the FeCN-PMS system, and $Fe^{2+}$ was only continued when part of the $Fe^{2+}$ was oxidized to $Fe^{3+}$ by PMS. The oxidation pathways of the dissolved iron ions are presented in Eq. (1) (Zheng et al., 2022).

$$Fe^{2+}+HSO_5^- \rightarrow Fe^{3+}+SO_4^{\bullet -}+OH^- \quad (1)$$

### 3.3.2. Generation and identification of ROS

Scavengers were added to convincingly demonstrate the ability of ROS to inactivate *M. aeruginosa*, in which FFA and L-histidine as quenchers for $^1O_2$. Fig. 6a illustrates the effects of the different scavengers. When L-histidine and FFA were added, the inactivation efficiency was significantly reduced. The reaction rate was also reduced when $C_2H_6O$ and IPA were added. Therefore, $^1O_2$ might be the dominant active species, followed by $SO_4^{\bullet -}$ and $^{\bullet}OH$. The ROS generation pathway in the FeCN-PMS system is shown in Eqs. (2)–(5) (Gao et al., 2022).

Moreover, $^1O_2$ in the FeCN-PMS system was reportedly not generated from $O_2^{\bullet -}$; however, FeCN tended to adsorb the O site of PMS, thereby promoting the oxidation of PMS to $SO_5^{\bullet -}$ via the loss of H atoms. This leads to a generation of $^1O_2$, as shown in Eqs. (6)–(8) (Zhang et al., 2021).

$$Fe(II)\text{-}CN+HSO_5^- \rightarrow Fe(III)\text{-}CN+SO_4^{\bullet -}+OH^- \quad (2)$$

$$SO_4^{\bullet -}+H_2O \rightarrow {}^{\bullet}OH+H^++SO_4^{2-} \quad (3)$$

$$Fe(III)\text{-}CN+ HSO_5^- \rightarrow Fe(II)\text{-}CN+ SO_4^{2-}+1/2\ O_2^{\bullet -}+H^+ \quad (4)$$

$$2\ O_2^{\bullet -}+2\ H_2O \rightarrow H_2O_2+OH^-+{}^1O_2 \quad (5)$$

$$HSO_5^- \rightarrow SO_5^{\bullet -}+H^++e^- \quad (6)$$

$$SO_5^{\bullet -}+SO_5^{\bullet -} \rightarrow S_2O_8^{2-}+{}^1O_2 \quad (7)$$

$$SO_5^{\bullet -}+SO_5^{\bullet -} \rightarrow 2SO_4^{2-}+{}^1O_2 \quad (8)$$

EPR spectra were used to determine the presence of the ROS generated by the FeCN-PMS system. The spectra of $SO_4^{\bullet -}$, $^{\bullet}OH$, $O_2^{\bullet -}$, and $^1O_2$ were separately obtained, indicating the presence of $SO_4^{\bullet -}$, $^{\bullet}OH$, $O_2^{\bullet -}$, and $^1O_2$. As shown in Fig. 6b, DMPO-$SO_4^{\bullet -}$ and DMPO-$^{\bullet}OH$ signals appeared in the EPR spectra. The characteristic signal of $O_2^{\bullet -}$ is shown in Fig. 6c. Similarly, the characteristic triplet state signal of 1:1:1 (TEMP-$^1O_2$) also appears in Fig. 6d. The intensity of all these signals increased from 5 to 10 min (Fig. S6), with $^1O_2$ showing the largest increase in intensity. These results indicate that ROS are continuously produced by the FeCN-PMS system and can inactivate algal cells via strong oxidation.

## 3.4. Degradation experiments of algal toxins

### 3.4.1. Simultaneous removal of algal cells and algal toxins

The rupture of algal cells is inevitably accompanied by the release of large amounts of algal toxins, which have a significant impact on other

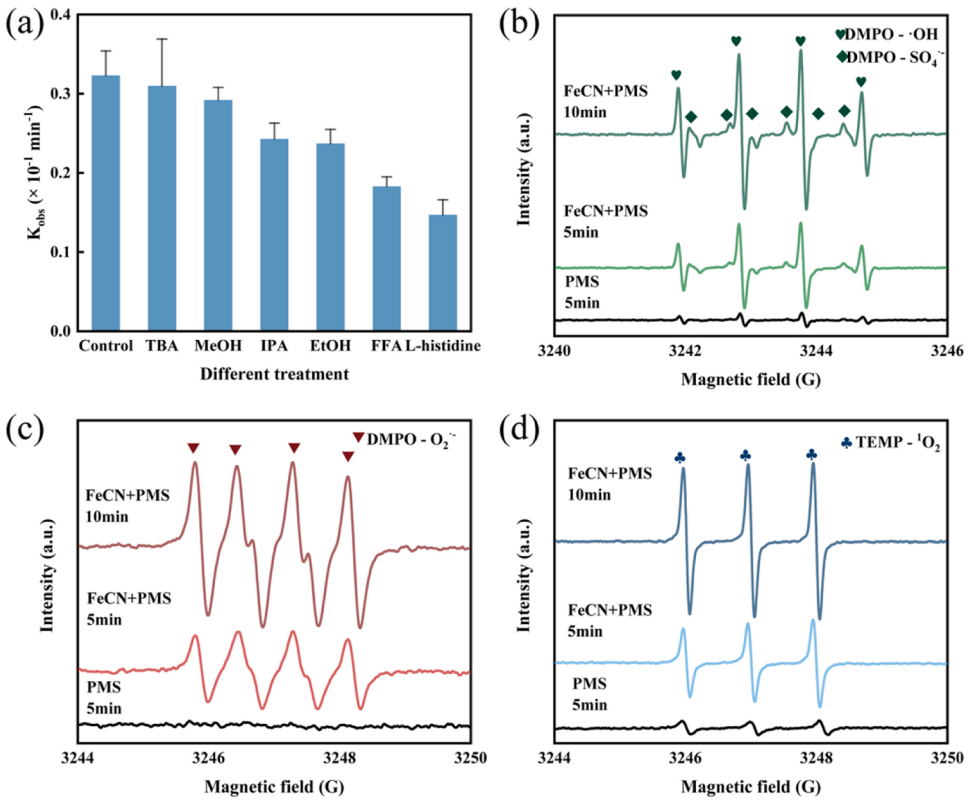


**Fig. 6.** (a) $K_{obs}$ of the FeCN-PMS system with different quenchers. The reacted solution initially contained approximately 0.60 mg·$L^{-1}$ of chlorophyll-*a*, 0.2 g·$L^{-1}$ of FeCN, and 0.33 mM of PMS; the scavenger concentration: 20.0 mM; EPR spectra: (b) $SO_4^{\bullet-}$ and $^{\bullet}OH$, (c) $O_2^{\bullet-}$, and (d) $^1O_2$.

organisms and the environment (Plaas and Paerl, 2021). Therefore, we evaluated the degradation of algal toxins by the FeCN-PMS system. Fig. 7a shows the variations in the MC-LR concentration at different reaction times. At 30 min, the released concentration of MC-LR exceeded the initial concentration, which was caused by the breaking of large number of algal cells releasing MC-LR. The MC-LR concentration gradually decreased. Finally, the released concentration of MC-LR was degraded by approximately 70% after 180 min. The relationship between algal toxin release and degradation is shown in Fig. S5, it is considered that algal toxin degradation and cell inactivation simultaneously occur owing to FeCN-PMS system. Considering that it is not possible to include only MC-LR, the degradation of NOD by the FeCN-PMS system was also evaluated. Similarly, the NOD concentration gradually decreased, reaching a degradation efficiency of approximately 80% at 180 min (Fig. 7b). Because of the simulated addition of NOD to the algal solution, there was no cell rupture or release of algal toxins compared with MC-LR degradation. Overall, the FeCN-PMS system not only inactivates algal cells but also effectively degrades algal toxins released from these cells.

### 3.4.2. *Reaction intermediates and possible degradation pathways*

Eight degradation intermediates of MC-LR ($m/z$ = 608.6, 429.3, 417.2, 414.7, 313.4, 279.2, 274.3, and 245.2) were identified and analyzed based on the LC-MS/MS results (Fig. S7 and Table S2). Fig. 8 shows the possible degradation pathways of MC-LR in the FeCN-PMS system. MC-LR is a cyclic heptapeptide compound with biological activities and is found in *Adda*, *Glu*, *Mdha*, *Ala*, *Leu*, *MeAsp*, *and Arg*. Reportedly, the double bond of the *Adda* side-chain hydroxylates forms a dihydroxy intermediate (A1–1, A1–2, and A1–3, $m/z$=1029.6). These dihydroxy intermediates continue to produce ketone derivatives (A2, $m/z$=835.4) owing to bond cleavage (Fan et al., 2022). In a first possible pathway, A3–1 ($m/z$=417.2) (Fotiou et al., 2013) is generated and

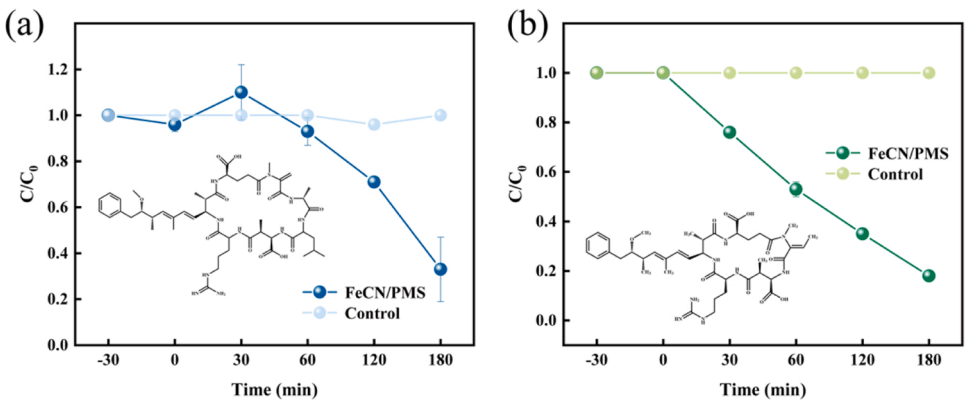


**Fig. 7.** Variations in (a) MC-LR and (b) NOD concentration in the FeCN-PMS system at 25 ± 1 °C.

oxidized to A4 ($m/z$=279.2) owing to the cleavage of the *Adaa–Arg* bond. In addition, ketone derivatives may generate A3–2 ($m/z$ = 274.3) (Fan et al., 2022) via oxidation and bond cleavage. In a second possible pathway, C–C cleavage and the hydroxylation of *Adda* generate B1 ($m/z$ = 414.7), and this continues through electron transfer and hydroxylation generating B2 ($m/z$ = 429.3) (Moon et al., 2017). In a third pathway, C–N cleavage and hydroxylation of *Glu* generate C1 ($m/z$=313.4), and this continues through electron transfer and bond cleavage generating C2 ($m/z$=245.2) (Moon et al., 2017). In a fourth possible pathway, the cleavage of the *Adda–Glu* bond generates D1 ($m/z$=608.6) (Xie et al., 2021). Finally, these intermediates can be further oxidized and degraded and are eventually completely mineralized to $CO_2$, $NO_3^-$, and $NH_4^+$ (Triantis et al., 2012), establishing the exceptional mineralization ability of the FeCN-PMS system for the MC-LR. NOD contains an *Adda* group similar to MC-LR, and it was found that the degradation of NOD begins with the cleavage of the *Adda–Arg* bond (Yuan et al., 2021). Subject to the current research context, no reliable evidence was found for verifying this test.

### 3.5. Proposed mechanism

A potential mechanism for the inactivation of cyanobacteria and degradation of algal toxins by the FeCN-PMS system is shown in Fig. 9. Two ROS generation pathways may exist for the heterogeneous oxidation technique (FeCN-PMS system): a radical pathway generating $SO_4^{\bullet -}$. and $^{\bullet}OH$ and non-radical pathway generating $^1O_2$ (Wang et al., 2020). For the radical pathway, Fe(II) and Fe(III) conversions at the FeCN surface activate PMS to produce $SO_4^{\bullet -}$. In addition, Fe(II) dissolves in the algal solution to form $Fe^{2+}$, which is consistent with the observations in Fig. S2. In addition, $Fe^{2+}$ can activate PMS to produce $SO_4^{\bullet -}$. For the non-radical pathway, Fe(II) on FeCN activates PMS to produce $O_2^{\bullet -}$, resulting in the production of $^1O_2$; Fe–N bond also drives the production of $^1O_2$ by PMS. ROS produced via these two pathways (primarily $^1O_2$ produced by non-radical pathways) are very harmful to algal cells, destroying cell integrity and viability. A large amount of released algal toxins is degraded to reduce their toxic effects on aquatic organisms. Moreover, the ROS-oxidized part of the EOMs reduces environmental pollution, which is consistent with the results shown in Fig. S1. Therefore, the FeCN-PMS system can efficiently inactivate harmful cyanobacteria while avoiding the environmental problems caused by the release of intracellular substances.

## 4. Conclusions

FeCN with high dispersibility was synthesized using $C_3H_6N_6$ and $C_3H_3N_3O_3$ as precursors. FeCN activated PMS to produce $^1O_2$, which

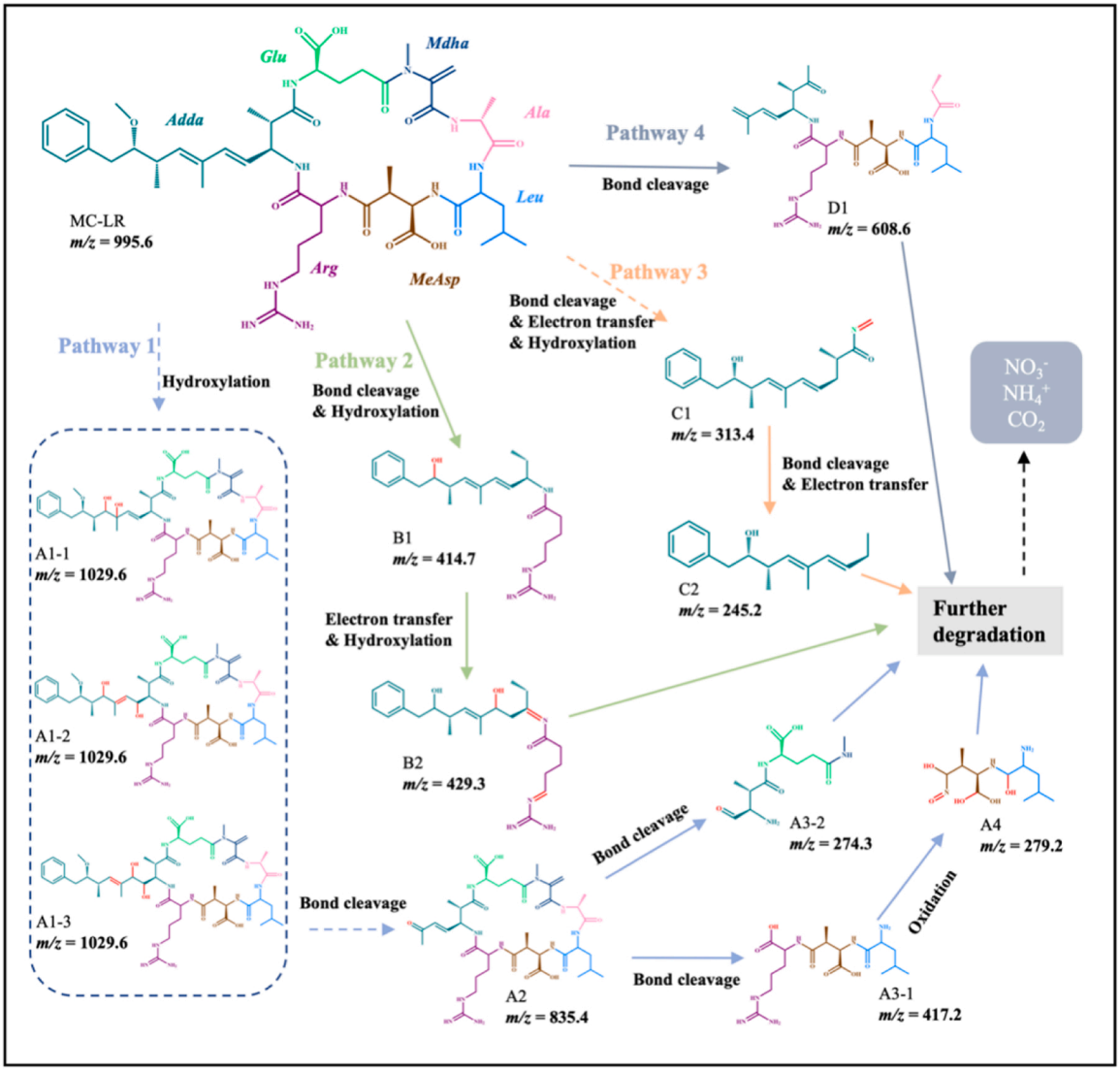


**Fig. 8.** Possible degradation pathway of MC-LR by the FeCN-PMS system.

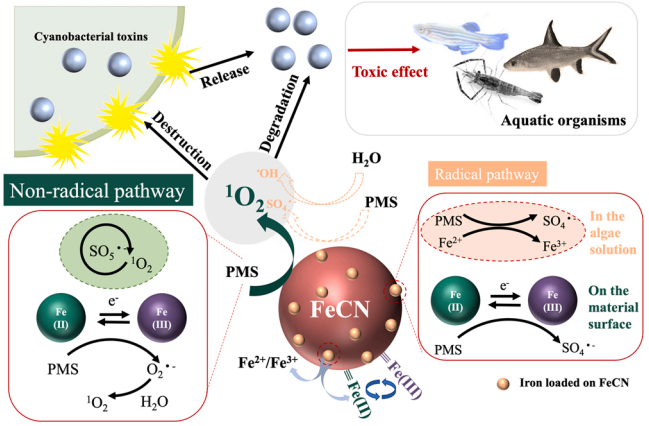


**Fig. 9.** Proposed mechanism of catalytic inactivation of cyanobacteria and degradation of cyanobacterial toxins by the FeCN-PMS system.

effectively inactivated *M. aeruginosa* and was effective against other cyanobacteria (*Nodularia harveyana*, *Oscillatoria* sp., and *Nostoc* sp.). Meanwhile, the system effectively reduced released algal toxins (MC-LR and NOD). The optimum dose of FeCN was 0.4 g $L^{-1}$ and that of PMS was 0.33 mM. The inactivation of *M. aeruginosa* was 92.77%, and the degradation rates of MC-LR and NOD were approximately 70% and 80%, respectively. The system was less affected by pH, and the inactivation rate still exceeded 70% under alkaline conditions. Humic acid had some effect on the system, causing a decrease in the inactivation rate. Finally, the mechanism of PMS activation by FeCN was revealed by ROS generation. After the free radical quenching experiments, $^1O_2$ was found to be the major ROS. Therefore, this heterogeneous oxidation technology should be efficient in simultaneously inactivating harmful cyanobacteria and degrading cyanobacterial toxins.

## CRediT authorship contribution statement

**Bingzhi Yu**: Investigation, Writing - review, Data curation, Visualization. **Xizi Li**: Investigation, Software, Resources, Revised. **Mengfan He:** Visualization, Revised, **Yan Li**: Data curation, Visualization. **Jiafeng Ding**: Formal analysis, Writing - original draft, Revised. **Yuchi Zhong**: Formal analysis, Visualization. **Hangjun Zhang**: Conceptualization, Writing - review and editing, Supervision.

## Declaration of Competing Interest

The authors declare that they have no known competing financial interests or personal relationships that could have appeared to influence the work reported in.

## Data availability

No data was used for the research described in the article.

## Acknowledgement

This study was supported by the National Natural Science Foundation of China (Grant No. 42107255), Natural Science Foundation of Zhejiang (Grant No. LQ21B070006), and Key Research & Development project of the Science and Technology Department of Zhejiang Province (Grant No. 2021C02048).

*Environmental implication*

Efficient treatment of harmful cyanobacterial blooms in eutrophication waters by safe and reliable strategies is a big challenge for reducing environmental health risks. This work investigated the inactivation of four harmful cyanobacteria by production of $^1O_2$. The inactivation efficiencies were high, and $^1O_2$ not only effectively destroyed the integrity of harmful cyanobacterial cells but also effectively degraded cyanobacterial toxins, Finally, a possible degradation pathway was proposed based on identified products. This study proposes an efficient and environment-friendly method for simultaneously inactivating harmful cyanobacteria and degrading algal toxins, thereby providing a reference basis for the treatment of harmful cyanobacterial blooms.

## Appendix A. Supporting information

Supplementary data associated with this article can be found in the online version at doi:10.1016/j.jhazmat.2022.129940.

## References

Cao, L.S., Wang, J.W., Wang, Z.P., Yu, S.W., Cheng, Y.J., Ma, J., Xie, P.C., 2022. Inactivation of Microcystis aeruginosa by peracetic acid combined with ultraviolet: performance and characteristics. Water Res. 208, 117847 https://doi.org/10.1016/j.watres.2021.117847.

Chen, P., Lei, B., Dong, X.A., Wang, H., Sheng, J.P., Cui, W., Li, J.Y., Sun, Y.J., Wang, Z. M., Dong, F., 2020. Rare-earth single-atom La-N charge-transfer bridge on carbon nitride for highly efficient and selective photocatalytic $CO_2$ reduction. ACS Nano 14, 10552–10561. https://doi.org/10.1021/acsnano.0c07083.

Chen, W., Westerhoff, P., Leenheer, J.A., Booksh, K., 2003. Fluorescence excitation-emission matrix regional integration to quantify spectra for dissolved organic matter. Environ. Sci. Technol. 37 (24), 5701–5710. https://doi.org/10.1021/es034354c.

Chu, L.L., Hou, X.X., Song, X.S., Zhao, X.X., 2022. Toxicological effects of different ionic liquids on growth, photosynthetic pigments, oxidative stress, and ultrastructure of Nostoc punctiforme and the combined toxicity with heavy metals. Chemosphere 298, 134273. https://doi.org/10.1016/j.chemosphere.2022.134273.

Di Mascio, P., Martinez, G.R., Miyamoto, S., Ronsein, G.E., Medeiros, M.H.G., Cadet, J., 2019. Singlet molecular oxygen reactions with nucleic acids, lipids, and proteins. Chem. Rev. 119 (3), 2043–2086. https://doi.org/10.1021/acs.chemrev.8b00554.

Duan, P.J., Pan, J.W., Du, W.Y., Yue, Q.Y., Gao, B.Y., Xu, X., 2021. Activation of peroxymonosulfate via mediated electron transfer mechanism on single-atom Fe catalyst for effective organic pollutants removal. Appl. Catal. B-Environ. 299, 120714 https://doi.org/10.1016/j.apcatb.2021.120714.

Fan, G.D., Chen, Z., Hong, L., Du, B.H., Yan, Z.S., Zhan, J.J., You, Y.F., Ning, R.S., Xiao, H.S., 2020. Simultaneous removal of harmful algal cells and toxins by a $Ag_2CO_3$-N: GO photocatalyst coating under visible light. Sci. Total Environ. 741 (1), 140341 https://doi.org/10.1016/j.scitotenv.2020.140341.

Fan, G.D., Lin, X., You, Y.F., Du, B.H., Li, X., Luo, J., 2022. Magnetically separable $ZnFe_2O_4/Ag_3PO_4/g\text{-}C_3N_4$ photocatalyst for inactivation of Microcystis aeruginosa: characterization, performance and mechanism. J. Hazard. Mater. 421, 126703 https://doi.org/10.1016/j.jhazmat.2021.126703.

Fang, G.G., Li, J.L., Zhang, C., Qin, F.Z., Luo, H.Z., Huang, C., Qin, D.Y., Ouyang, Z.L., 2022. Periodate activated by manganese oxide/biochar composites for antibiotic degradation in aqueous system: combined effects of active manganese species and biochar. Environ. Pollut. 300, 118939 https://doi.org/10.1016/j.envpol.2022.118939.

Fotiou, T., Triantis, T.M., Kaloudis, T., Pastrana-Martinez, L.M., Likodimos, V., Falaras, P., Silva, A.M.T., Hiskia, A., 2013. Photocatalytic degradation of microcystin-LR and off-odor compounds in water under UV-A and solar light with a nanostructured photocatalyst based on reduced graphene oxide-$TiO_2$ composite. identification of intermediate products. Ind. Eng. Chem. Res. 52 (39), 13991–14000. https://doi.org/10.1021/ie400382r.

Gao, D.X., Lu, Y.R., Chen, Y.P., Bao, M.Y., Xu, N., 2022. Novel $CoFe_2P_x$ derived from $CoFe_2O_4$ for efficient peroxymonosulfate activation: Switching the reaction route and suppressing metal leaching. Appl. Catal. B-Environ. 309, 121234 https://doi.org/10.1016/j.apcatb.2022.121234.

Guo, X.N., Zhu, A., Chen, R.S., 2021. China's algal bloom suffocates marine life. Science 373 (6556), 751-751. https://doi.org/10.1126/science.abl5774.

Guo, Y.F., Li, J., Yuan, Y.P., Li, L., Zhang, M.Y., Zhou, C.Y., Lin, Z.Q., 2016. A rapid microwave-assisted thermolysis route to highly crystalline carbon nitrides for efficient hydrogen generation. Angew. Chem. Int. Ed. 55 (47), 14693–14697. https://doi.org/10.1002/anie.201608453.

Hamblin, M.R., 2016. Antimicrobial photodynamic inactivation: a bright new technique to kill resistant microbes. Curr. Opin. Microbiol. 33, 67–73. https://doi.org/10.1016/j.mib.2016.06.008.

He, J.K., Huang, J.Y., Wang, Z.W., Liu, Z., Chen, Y., Su, R.D., Ni, X.Y., Li, Y.W., Xu, X., Zhou, W.Z., Gao, B.Y., Li, Q., 2022. The enhanced catalytic degradation of sulfamethoxazole over Fe@nitrogen-doped carbon-supported nanocomposite: Insight into the mechanism. Chem. Eng. J. 439, 135784 https://doi.org/10.1016/j.cej.2022.135784.

He, X.H., Wu, P., Wang, S.L., Wang, A.Z., Wang, C.L., Ding, P., 2021. Inactivation of harmful algae using photocatalysts: mechanisms and performance. J. Clean. Prod. 289, 125755 https://doi.org/10.1016/j.jclepro.2020.125755.

Ho, J.C., Michalak, A.M., Pahlevan, N., 2019. Widespread global increase in intense lake phytoplankton blooms since the 1980s. Nature 574 (7780), 667–670. https://doi.org/10.1038/s41586-019-1648-7.

Hoang, N.T., Nguyen, V.T., Minh Tuan, N.D., Manh, T.D., Le, P.-C., Van Tac, D., Mwazighe, F.M., 2022. Degradation of dyes by UV/Persulfate and comparison with other UV-based advanced oxidation processes: kinetics and role of radicals. Chemosphere 298, 134197. https://doi.org/10.1016/j.chemosphere.2022.134197.

Huang, J.Z., Jones, A., Waite, T.D., Chen, Y.L., Huang, X.P., Rosso, K.M., Kappler, A., Mansor, M., Tratnyek, P.G., Zhang, H.C., 2021a. Fe(II) Redox Chemistry in the Environment. Chem. Rev. 121 (13), 8161–8233. https://doi.org/10.1021/acs.chemrev.0c01286.

Huang, Y.R., Zhang, W.J., Li, L., Wei, X.M., Li, H.Z., Gao, N.Y., Yao, J.J., 2021b. Evaluation of ultrasound as a preventative algae-controlling strategy: Degradation behaviors and character variations of algal organic matter components during sonication at different frequency ranges. Chem. Eng. J. 426, 130891 https://doi.org/10.1016/j.cej.2021.130891.

Huisman, J., Codd, G.A., Paerl, H.W., Ibelings, B.W., Verspagen, J.M.H., Visser, P.M., 2018. Cyanobacterial blooms. Nat. Rev. Microbiol. 16 (8), 471–483. https://doi.org/10.1038/s41579-018-0040-1.

Huo, X.C., Chang, D.W., Tseng, J.H., Burch, M.D., Lin, T.F., 2015. Exposure of Microcystis aeruginosa to hydrogen peroxide under light: kinetic modeling of cell rupture and simultaneous microcystin degradation. Environ. Sci. Technol. 49 (9), 5502–5510. https://doi.org/10.1021/acs.est.5b00170.

Jeon, B.S., Han, J., Kim, S.K., Oh, H.C., Park, H.D., 2015. The removal of Microcystis ichthyoblabe cells and its hepatotoxin microcystin-LR during electrooxidation process using Pt/Ti electrodes. J. Environ. Sci. Heal. A 50 (6), 563–570. https://doi.org/10.1080/10934529.2015.994942.

Jimenez, L.D.Q., Guzman-Guillen, R., Catunescu, G.M., Campos, A., Vasconcelos, V., Jos, A., Camean, A.M., 2020. A new method for the simultaneous determination of cyanotoxins (Microcystins and Cylindrospermopsin) in mussels using SPE-UPLC-MS/MS. Environ. Res. 185, 109284 https://doi.org/10.1016/j.envres.2020.109284.

Li, X.D., Wu, B., Zhang, Q., Liu, Y.Q., Wang, J.Q., Li, F.S., Ma, F.J., Gu, Q.B., 2020a. Complexation of humic acid with Fe ions upon persulfate/ferrous oxidation: Further insight from spectral analysis. J. Hazard. Mater. 399, 123071 https://doi.org/10.1016/j.jhazmat.2020.123071.

Li, Y., Li, J., Pan, Y., Xiong, Z., Yao, G., Xie, R., Lai, B., 2020b. Peroxymonosulfate activation on $FeCo_2S_4$ modified g-$C_3N_4$ ($FeCo_2S_4$-CN): Mechanism of singlet oxygen evolution for nonradical efficient degradation of sulfamethoxazole. Chem. Eng. J. 384, 123361 https://doi.org/10.1016/j.cej.2019.123361.

Liu, Q., Guo, Y.R., Chen, Z.H., Zhang, Z.G., Fang, X.M., 2016. Constructing a novel ternary Fe(III)/graphene/g-$C_3N_4$ composite photocatalyst with enhanced visible-light driven photocatalytic activity via interfacial charge transfer effect. Appl. Catal. B-Environ. 183, 231–241. https://doi.org/10.1016/j.apcatb.2015.10.054.

Liu, T.Y., Wang, C., Han, Y.Z., Bai, C., Ren, H.T., Liu, Y., Han, X., 2022. Oxidative polymerization of bisphenol A (BPA) via H-abstraction by Bi2.15WO6 and persulfate: Importance of the surface complexes. Chem. Eng. J. 435, 134816 https://doi.org/10.1016/j.cej.2022.134816.

Liu, Y., Guo, H.G., Zhang, Y.L., Tang, W.H., Cheng, X., Li, W., 2018. Heterogeneous activation of peroxymonosulfate by sillenite $Bi_{25}FeO_{40}$: singlet oxygen generation and degradation for aquatic levofloxacin. Chem. Eng. J. 343, 128–137. https://doi.org/10.1016/j.cej.2018.02.125.

Mao, S., Liu, C., Wu, Y., Xia, M.Z., Wang, F.Y., 2022. Porous P, Fe-doped g-$C_3N_4$ nanostructure with enhanced photo-Fenton activity for removal of tetracycline hydrochloride: mechanism insight, DFT calculation and degradation pathways. Chemosphere 291, 133039. https://doi.org/10.1016/j.chemosphere.2021.133039.

Mi, X.Y., Wang, P.F., Xu, S.Z., Su, L.N., Zhong, H., Wang, H.T., Li, Y., Zhan, S.H., 2021. Almost 100% peroxymonosulfate conversion to singlet oxygen on single-atom CoN2 +2 sites. Angew. Chem. Int. Ed. 60 (9), 4588–4593. https://doi.org/10.1002/anie.202014472.

Miao, J., Duan, X.G., Li, J., Dai, J., Liu, B., Wang, S.B., Zhou, W., Shao, Z.P., 2019. Boosting performance of lanthanide magnetism perovskite for advanced oxidation through lattice doping with catalytically inert element. Chem. Eng. J. 355, 721–730. https://doi.org/10.1016/j.cej.2018.08.192.

Moon, B.-R., Kim, T.-K., Kim, M.-K., Choi, J., Zoh, K.-D., 2017. Degradation mechanisms of Microcystin-LR during UV-B photolysis and UV/$H_2O_2$ processes: byproducts and pathways. Chemosphere 185, 1039–1047. https://doi.org/10.1016/j.chemosphere.2017.07.104.

Paerl, H.W., Gardner, W.S., Havens, K.E., Joyner, A.R., McCarthy, M.J., Newell, S.E., Qin, B.Q., Scott, J.T., 2016. Mitigating cyanobacterial harmful algal blooms in aquatic ecosystems impacted by climate change and anthropogenic nutrients. Harmful Algae 54, 213–222. https://doi.org/10.1016/j.hal.2015.09.009.

Peng, X.M., Wu, J.Q., Zhao, Z.L., Wang, X., Dai, H.L., Xu, L., Xu, G.P., Jian, Y., Hu, F.P., 2022. Activation of peroxymonosulfate by single-atom Fe-g-$C_3N_4$ catalysts for high efficiency degradation of tetracycline via nonradical pathways: Role of high-valent iron-oxo species and Fe-Nx sites. Chem. Eng. J. 427, 130803 https://doi.org/10.1016/j.cej.2021.130803.

Perillo, V.L., La Colla, N.S., Pan, J., Serra, A.V., Botte, S.E., Cuadrado, D.G., 2022. Epibenthic microbial mats behavior as phosphorus sinks or sources in relation to biological and physicochemical conditions. J. Environ. Manag. 314, 115079 https://doi.org/10.1016/j.jenvman.2022.115079.

Plaas, H.E., Paerl, H.W., 2021. Toxic cyanobacteria: a growing threat to water and air quality. Environ. Sci. Technol. 55 (1), 44–64. https://doi.org/10.1021/acs.est.0c06653.

Song, Q., Zhang, D., Niu, X., Li, Y., Ma, J., Fan, Y., Zhou, S., 2020. Effective removal of Microcystis aeruginosa and microcystins by integrated pre-oxidation and coagulation: an environmental and economical way. Int. J. Environ. Sci. Te. 17 (8), 3761–3770. https://doi.org/10.1007/s13762-020-02732-x.

Sun, P.F., Yu, H.J., Liu, T.T., Li, Y.S., Wang, Z.S., Xiao, Y.F., Dong, X.P., 2022. Efficiently photothermal conversion in a MnOx-based monolithic photothermocatalyst for gaseous formaldehyde elimination. Chin. Chem. Lett. 33 (5), 2564–2568. https://doi.org/10.1016/j.cclet.2021.09.050.

Tan, P.L., 2016. Active phase, catalytic activity, and induction period of Fe/zeolite material in nonoxidative aromatization of methane. J. Catal. 338, 21–29. https://doi.org/10.1016/j.jcat.2016.01.027.

Triantis, T.M., Fotiou, T., Kaloudis, T., Kontos, A.G., Falaras, P., Dionysiou, D.D., Pelaez, M., Hiskia, A., 2012. Photocatalytic degradation and mineralization of microcystin-LR under UV-A, solar and visible light using nanostructured nitrogen doped $TiO_2$. J. Hazard. Mater. 211, 196–202. https://doi.org/10.1016/j.jhazmat.2011.11.042.

Wang, H.Z., Guo, W.Q., Liu, B.H., Wu, Q.L., Luo, H.C., Zhao, Q., Si, Q.S., Sseguya, F., Ren, N.Q., 2019. Edge-nitrogenated biochar for efficient peroxydisulfate activation: An electron transfer mechanism. Water Res. 160, 405–414. https://doi.org/10.1016/j.watres.2019.05.059.

Wang, H.Z., Guo, W.Q., Liu, B.H., Si, Q.S., Luo, H.C., Zhao, Q., Ren, N.Q., 2020. Sludge-derived biochar as efficient persulfate activators: Sulfurization-induced electronic structure modulation and disparate nonradical mechanisms. Appl. Catal. B-Environ. 279, 119361 https://doi.org/10.1016/j.apcatb.2020.119361.

Wang, S.Z., Wang, J.L., 2022. High efficient activation of peroxymonosulfate by $Co_9S_8$ anchored in N, S, O co-doped carbon composite for degradation of sulfamethoxazole: effect of sulfur precursor and sulfur doping content. Chem. Eng. J. 434, 134824 https://doi.org/10.1016/j.cej.2022.134824.

Xia, J.H., Zhang, H., Ding, S.X., Li, C.Y., Ding, J.C., Lu, J., 2018. Promotion by humus-reducing bacteria for the degradation of $UV_{254}$ absorbance in reverse-osmosis concentrates pretreated with $O_3$-assisted UV-Fenton method. Environ. Technol. 39 (17), 2178–2184. https://doi.org/10.1080/09593330.2017.1351497.

Xiao, R.Y., Luo, Z.H., Wei, Z.S., Luo, S., Spinney, R., Yang, W.C., Dionysiou, D.D., 2018. Activation of peroxymonosulfate/persulfate by nanomaterials for sulfate radical-based advanced oxidation technologies. Curr. Opin. Chem. Eng. 19, 51–58. https://doi.org/10.1016/j.coche.2017.12.005.

Xie, G.Y., Hu, X.J., Du, Y.X., Jin, Q., Liu, Y., Tang, C.F., Hu, X., Li, G.Y., Chen, Z.F., Zhou, D.X., Wang, H., 2021. Light-driven breakdown of microcystin-LR in water: A critical review. Chem. Eng. J. 417, 129244 https://doi.org/10.1016/j.cej.2021.129244.

Yan, J.C., Gao, W.G., Dong, M.G., Han, L., Qian, L.B., Nathanail, C.P., Chen, M.F., 2016. Degradation of trichloroethylene by activated persulfate using a reduced graphene oxide supported magnetite nanoparticle. Chem. Eng. J. 295, 309–316. https://doi.org/10.1016/j.cej.2016.01.085.

Yan, Z.D., Yang, X.N., Lynch, I., Cui, F.Y., 2022. Comparative evaluation of the mechanisms of toxicity of graphene oxide and graphene oxide quantum dots to blue-green algae Microcystis aeruginosa in the aquatic environment. J. Hazard. Mater. 425, 127898 https://doi.org/10.1016/j.jhazmat.2021.127898.

Yaraki, M.T., Liu, B., Tan, Y.N., 2022. Emerging strategies in enhancing singlet oxygen generation of nano-photosensitizers toward advanced phototherapy. Nano-Micro Lett. 14 (1), 123. https://doi.org/10.1007/s40820-022-00856-y.

Yu, H.R., Wu, Z.J., Zhang, X.L., Qu, F.S., Wang, P., Liang, H., 2019. Characterization of fluorescence foulants on ultrafiltration membrane FA using front-face excitation-emission matrix (FF-EEM) spectroscopy: Fouling evolution and mechanism analysis. Water Res. 148, 546–555. https://doi.org/10.1016/j.watres.2018.10.041.

Yuan, M.X., Ding, Q., Sun, R.L., Zhang, J., Yin, L.H., Pu, Y.P., 2021. Biodegradation of Nodularin by a Microcystin-degrading bacterium: performance, degradation pathway, and potential application. Toxins 13 (11), 813. https://doi.org/10.3390/toxins13110813.

Zetterholm, S.G., Gurtowski, L., Roberts, J.L., McLeod, S., Fernando, B.M., Griggs, C.S., 2022. Graphene-Mediated removal of Microcystin-LR in chitosan/graphene composites for treatment of harmful algal blooms. Chemosphere 300, 134583. https://doi.org/10.1016/j.chemosphere.2022.134583.

Zhang, L.S., Jiang, X.H., Zhong, Z.A., Tian, L., Sun, Q., Cui, Y.T., Lu, X., Zou, J.P., Luo, S. L., 2021. Carbon nitride supported high-loading Fe single-atom catalyst for activating of peroxymonosulfate to generate $^1O_2$ with 100% selectivity. Angew. Chem. Int. Ed. 60 (40), 21751–21755. https://doi.org/10.1002/anie.202109488.

Zhang, Y., Chen, X., Cui, M.S., Guo, Z., Chen, Y.H., Cui, K.P., Ding, Z.G., Weerasooriya, R., 2022. Binding Fe-doped g-$C_3N_4$ on the porous diatomite for efficient degradation of tetracycline via photo-Fenton process. J. Environ. Chem. Eng. 10 (3), 107406 https://doi.org/10.1016/j.jece.2022.107406.

Zhang, H.J., Yu, B.Z., Li, X.Z., Li, Y., Zhong, Y.C., Ding, J.F., 2022. Inactivation of Microcystis aeruginosa by peroxydisulfate activated with single-atomic iron catalysis: Efficiency and mechanisms. J. Environ. Chem. Eng. 10 (5), 108310. https://doi.org/10.1016/j.jece.2022.108310.

Zhao, G.S., Ding, J., Ren, J.Y., Zhao, Q.L., Gao, Q.W., Wang, K., Wei, L.L., Chen, X.Q., Zhou, F.Y., Dionysiou, D.D., 2022. Insight into the visible light activation of sulfite by Fe/g-$C_3N_4$ with rich N vacancies for pollutant removal and sterilization: A novel approach for enhanced generation of oxysulfur radical. Chem. Eng. J. 438, 135663 https://doi.org/10.1016/j.cej.2022.135663.

Zhao, Y., Huang, B., An, H.Z., Dong, G.J., Feng, J., Wei, T., Ren, Y.M., Ma, J., 2021a. Enhanced activation of peroxymonosulfate by Sr-doped $LaFeO_3$ perovskite for Orange I degradation in the water. Sep. Purif. Technol. 256, 117838 https://doi.org/10.1016/j.seppur.2020.117838.

Zhao, Y.F., Zhou, H., Zhu, X.R., Qu, Y.T., Xiong, C., Xue, Z.G., Zhang, Q.W., Liu, X.K., Zhou, F.Y., Mou, X.M., Wang, W.Y., Chen, M., Xiong, Y., Lin, X.G., Lin, Y., Chen, W. X., Wane, H.J., Jiang, Z., Zheng, L.R., Yao, T., Dong, J.C., Wei, S.Q., Huang, W.X., Gu, L., Luo, J., Li, Y.F., Wu, Y.E., 2021b. Simultaneous oxidative and reductive

reactions in one system by atomic design. Nat. Catal. 4, 134–143. https://doi.org/10.1038/s41929-020-00563-0.

Zheng, X.X., Niu, X.J., Zhang, D.Q., Ye, X.Y., Ma, J.L., Lv, M.Y., Lin, Z., 2022. Removal of Microcystis aeruginosa by natural pyrite-activated persulfate: Performance and the significance of iron species. Chem. Eng. J. 428, 132565 https://doi.org/10.1016/j.cej.2021.132565.

Zhou, L., Cai, M., Zhang, X., Cui, N.X., Chen, G.F., Zou, G.Y., 2020. In-situ nitrogen-doped black $TiO_2$ with enhanced visible-light-driven photocatalytic inactivation of Microcystis aeruginosa cells: Synthesization, performance and mechanism. Appl. Catal. B-Environ. 272, 119019 https://doi.org/10.1016/j.apcatb.2020.119019.

Zhu, X.Q., Dao, G.H., Tao, Y., Zhan, X.M., Hu, H.Y., 2021. A review on control of harmful algal blooms by plant-derived allelochemicals. J. Hazard. Mater. 401, 123403 https://doi.org/10.1016/j.jhazmat.2020.123403.